



Full length article

Carbon and strain partitioning in a quenched and partitioned steel containing ferrite

Xiaodong Tan ^{a,*}, Dirk Ponge ^{b,**}, Wenjun Lu ^b, Yunbo Xu ^c, Xiaolong Yang ^d, Xi Rao ^a, Di Wu ^c, Dierk Raabe ^b^a Faculty of Materials and Energy, Southwest University, Chongqing, 400715, PR China^b Max-Planck-Institut für Eisenforschung GmbH, Düsseldorf, 40237, Germany^c State Key Laboratory of Rolling and Automation, Northeastern University, Shenyang, 110819, PR China^d HBIS Group Tangsteel Company Technical Center, Tangshan, 063016, PR China

ARTICLE INFO

Article history:

Received 29 July 2018

Received in revised form

12 November 2018

Accepted 10 December 2018

Available online 12 December 2018

Keywords:

Q&P steel

Carbon partitioning

Strain partitioning

Atom probe tomography

Digital image correlation

TRIP effect

ABSTRACT

We applied a hot rolling direct quenching and partitioning (HDQ&P) process to a low-C low-Si Al-added steel and obtained a Q&P steel containing 40 vol % of ferrite. Microstructure characterization was performed by means of SEM, EBSD, TEM and XRD. Atomic-scale characterization of carbon partitioning among the phases was carried out by atom probe tomography (APT). The carbon distribution in the retained austenite and near the martensite/retained austenite interfaces was quantitatively analyzed to study its partitioning behavior. The macroscopic strain distribution evolution across the tensile sample surface was investigated using macro digital image correlation (DIC) analysis. Combining these results with joint micro-DIC and EBSD analysis during quasi in-situ tensile testing, we investigated the strain partitioning among the different phases and the TRIP effect. Coupling of these results enabled us to reveal the relation among carbon partitioning, strain partitioning and the TRIP effect. The large blocky retained austenite with a side length of about 300–600 nm located near the ferrite/martensite (F/M) interfaces has low stability and transforms to martensite during the early deformation stages, i.e. at average strain below 21%. The retained austenite films in the centers of the martensite regions are more stable. The carbon distribution in both, the martensite and the retained austenite are inhomogeneous, with 0.5–2.0 at. % in the martensite and 4.0–7.5 at. % in the retained austenite. Strong carbon concentration gradients of up to 1.1 at. %/nm were observed near the martensite/retained austenite interfaces. The large blocky retained austenite (300–600 nm in side length) near the F/M interfaces has 1.5–2.0 at. % lower carbon content than that in the narrow retained austenite films (20–150 nm in thickness). The ferrite is soft and deforms prior to the martensite. The strain distribution in ferrite and martensite is inhomogeneous, varying by up to 20% within the same phase at an average strain of about 20%. Ferrite deformation is the main origin of ductility of the material. The balance between ferrite fraction and martensite morphology controls the TRIP effect and its efficiency in reaching a suited combination of strength and ductility. Reducing the ferrite volume fraction and softening the martensite by coarsening and polygonization can enhance the strain carried by the martensite, thus promoting more retained austenite in the martensite regions enabling a TRIP effect. The enhancement of the TRIP effect and the decrease of the strain contrast between ferrite and martensite jointly optimize the micromechanical deformation compatibility of the adjacent phases, thus improving the material's ductility.

© 2018 Acta Materialia Inc. Published by Elsevier Ltd. All rights reserved.

1. Introduction

To meet the requirements of both light weight and safety of vehicles, advanced high strength steels (AHSS) with high strength and ductility are required [1–3]. Speer et al. proposed a quenching and partitioning (Q&P) process, which leads to steel microstructures composed of martensite and retained austenite, so-called

* Corresponding author. Faculty of Materials and Energy, Southwest University, Tiansheng-Road 2, Beibei District, Chongqing, 400715, PR China.

** Corresponding author. Max-Planck-Institut für Eisenforschung GmbH, Max-Planck-Str. 1, Düsseldorf, 40237, Germany.

E-mail addresses: tanxd2017@swu.edu.cn, tanxiaodong163@163.com (X. Tan), d.ponge@mpie.de (D. Ponge).

Q&P steel [4–6]. In the Q&P process, the steel is quenched into a range between the martensite start (M_s) temperature and the martensite finish (M_f) temperature and held in a regime to stabilize untransformed austenite via the partitioning of carbon that evades from the initially formed martensite [7,8]. As shown in earlier studies, with limited addition of C, Si, Mn and Al, Q&P steels provide a good combination of strength and elongation (up to 1500 MPa tensile strength at 25% deformation to fracture) [9–11]. Thus, numerous studies have been carried out on the structure-property relations of Q&P steels [12–17]. Most of these works focused on thermodynamic models to explain the carbon partitioning, such as the constrained carbon equilibrium (CCE) model, as well as on Q&P process improvement and structure-property characteristics [18–26].

In recent years, various metallurgical aspects have been involved in the Q&P process design, leading to a number of Q&P process variants and different kinds of Q&P steels [18,27–32]. Most of these steels have a martensite matrix, providing a high tensile strength of up to 2000 MPa. Yet, such martensite/austenite dual-phase Q&P steels also have limited formability [15,33,34]. For solving this challenge, ferrite was introduced as a soft and compliant phase into Q&P steels [35,36]. Some results showed that the introduction of ferrite to an amount of 30–40 vol % can effectively decrease the yield strength (YS) and enhance the ductility of Q&P steels without significant reduction of its ultimate tensile strength (UTS) [37]. Some studies attributed the excellent ductility of these alloy variants to the ferrite deformation and the transformation induced plasticity (TRIP) effect [38]. Some recent studies discussed the interplay of the introduction of ferrite and the TRIP effect associated with the retained and partition-stabilized austenite [12,37,39,40]. It was argued that the introduction of ferrite alone cannot effectively improve the TRIP effect, although it can partly enhance the austenite stability and influence the morphology and distribution of the retained austenite [39]. For multi-phase steels consisting of a soft and a hard phase, the strain partitioning among the phases can directly influence the deformation homogeneity and the local stress/strain state of the structures near the phase interfaces [39,41–45]. Since retained austenite can be tuned in its stability to trigger a TRIP effect at a certain desired deformation level, the strain partitioning between ferrite and martensite may have a significant influence on the TRIP effect in these materials [46].

To further explore and utilize the ductility potential of ferrite-containing Q&P steel, it is thus important to better understand what the main ductility origin of these materials is. This involves several key issues. The first question is how substantial the ductilization contributed by the TRIP effect is. The second one is how strain partition among the phases works. The third one is how this mechanical partitioning affects the TRIP effect. On the basis of these questions we try to identify how these features can altogether be utilized to enhance the sequence and effectiveness in the activation of the TRIP effect for designing Q&P steels with improved strength-ductility balance [47,48]. We study these aspects by using quasi in-situ tensile tests in conjunction with microscopic digital image correlation (micro-DIC) based microscopic strain mapping and electron backscatter diffraction (EBSD) based microstructure mapping.

Carbon is the most effective element for austenite stabilization and it is also the most efficient one in controlling the hardness of the different phases [49]. The hardness difference among adjacent phases has significant influence on strain partitioning. Thus, it is important to also investigate the difference in carbon content among adjacent phases in ferrite-containing Q&P steel. So far, X-ray diffraction (XRD) has been the most widely used method for quantifying carbon partitioning [50–53]. However, it can only

distinguish phases with different lattice structure such as fcc and bcc. It cannot detect the carbon content difference between ferrite and low-carbon martensite (with a carbon content below 0.2 wt %) or among retained austenite grains with different size, location, grain neighborhood and morphology. Also, XRD cannot resolve local partitioning gradients across hetero-interfaces. Although some studies utilized atom probe tomography (APT) for investigating carbon partitioning in Q&P steels, they mostly focused on the martensite/austenite interface [26,54,55]. Yet, for the reasons outlined above, it is important to also systematically study the difference in carbon content among other adjacent phases and also the carbon distribution near the phase interfaces in ferrite-containing Q&P steel.

In the present paper, a hot rolling direct quenching and partitioning (HDQ&P) process was applied to a low-C low-Si Al-added steel. Ferrite was introduced into the steel by controlling the hot rolling process. An atomic-scale analysis of carbon partitioning among ferrite, martensite and retained austenite was carried out by means of APT. By conducting quasi in-situ tensile testing, the TRIP effect and strain partitioning features among the phases were investigated using EBSD and micro-DIC. The resulting local strain maps and the associated observation of the local TRIP effect were analyzed in connection to the ferrite fraction and martensite morphology in the analyzed region. Based on the strain maps and the associated EBSD results, we reveal the main origin of the ductility in terms of the chemical partitioning, micromechanical strain partitioning, the TRIP effect and the nature of adjacent phases in ferrite-containing Q&P steel. We also propose a microstructure design strategy in terms of a ferrite/martensite (F/M) fraction ratio adjustment and martensite morphology control to optimize the TRIP effect and the strength-ductility combination in these materials.

2. Experimental details

The steel with its chemical composition as shown in Table 1 was melted in a vacuum induction furnace and then cast into a 150-kg ingot. The ingot was then forged into a slab with a cross section of 40 mm × 40 mm. The critical temperatures of the phase transformations were measured by a Formastor-FII (FTF-340) dilatometer and the corresponding results are shown in Table 2. The heating rate used for probing the A_{c1} & A_{c3} temperatures was 0.05 °C/s. The critical quench rate for the martensite transformation in this steel was about –40 °C/s.

For hot rolling the slab was fully austenitized at 1200 °C for 2 h and then hot-rolled to 4 mm through 7 passes with a finish rolling temperature of about 910 °C. After air-cooling to about 760 °C, the sheet was directly quenched to 370 °C with a cooling rate of about –195 °C/s and subsequently partitioned in a furnace at a temperature of 350 °C for 5 min and finally air-cooled to room temperature. The actual carbon partitioning was achieved in a continuous cooling process from 370 °C to 350 °C and the cooling rate was about –0.05 °C/s.

Secondary electron (SE) image and EBSD analysis was carried out on a JEOL-JSM-6500F field emission scanning electron microscope (SEM). Transmission electron microscopy (TEM) was performed using a TECNAI G220 microscope at an operating voltage of 200 kV. Samples for SE imaging were ground, mechanically

Table 1
Chemical composition of the tested steel (wt. %).

| C | Si | Mn | Al | P | Fe |
|------|------|------|------|------|---------|
| 0.18 | 0.53 | 1.95 | 1.46 | 0.08 | Balance |

Table 2

Critical temperatures of the phase transformations in the tested steel (°C).

| A_{c1} | A_{c3} | A_{r1} | A_{r3} | M_s | M_f |
|----------|----------|----------|----------|-------|-------|
| 712 | 1037 | 634 | 914 | 421 | 172 |

polished and etched in 4 vol % nital solution for 10 s. For EBSD analysis, the samples were mechanically ground and polished, followed by colloidal silica (OPS) polishing to remove the deformed surface layer. EBSD measurements were carried out at 15 kV at a step size of 50 nm. The iron-bcc phase and the iron-fcc phase were chosen for EBSD based phase identification. Samples for TEM observation were firstly ground to a thickness of 40 μm then electro-polished at -20°C in a twin-jet machine.

To investigate the mechanical properties and macro strain distribution across the sample surface during deformation, tensile testing in conjunction with macro-DIC analysis was carried out at a crosshead speed of 4 $\mu\text{m/s}$. The strain distribution during deformation was analyzed using the ARAMIS software (GOM GmbH). For the tensile tests, samples with a thickness of 1.5 mm, width of 2 mm and length of 4 mm were prepared along the rolling direction. XRD analysis was performed on local regions with different strain in the fractured sample. The XRD measurements of these local regions were carried out on a Bruker D8_MU diffractometer with $\text{CoK}\alpha_1$ radiation at room temperature (Beam diameter: 0.3 mm; $\Delta 2\theta = 0.05^\circ$; Integration/counting time = 60 s/frame; Power setup: 40 kV/40 mA; Measurement range: 4 frames; Chi integration range: $\pm 15^\circ$). The sample surface selected for the XRD measurement was finally polished with OPS to release the residual stress.

Atomic-scale element distribution measurements in the different phases were conducted by APT. Site specific APT specimens were prepared on a dual-beam focused ion beam (FIB) (FEI, Helios Nano-Lab 600i), based on the EBSD results. APT characterization was conducted on a LEAP 3000X HR instrument (Cameca) in voltage mode at a base temperature of 75 K (-198°C). The pulse fraction and the pulse rate were 15% and 200 kHz, respectively. Reconstruction was carried out using the software Cameca IVAS[®] [56].

Quasi in-situ tensile tests in combination with micro-DIC and EBSD mapping were carried out to investigate the strain partitioning among the different phases and to map the TRIP effect during deformation. Tensile samples with gauge dimensions of 4 mm \times 2 mm \times 1.5 mm were prepared by spark erosion machining. The sample surfaces were polished with OPS, following a conventional metallographic grinding and diamond polishing procedure. Prior to the deformation experiments, a large field-of-view (40 μm \times 80 μm) EBSD measurement was performed on JEOL-JSM-6500F field emission SEM to identify the phases in the local regions of interest (ROIs). An acceleration voltage of 15 kV with a step size of 50 nm was chosen to enable high resolution. After the EBSD measurement, a 20 min plasma cleaning was conducted to remove carbon contamination. Subsequently, a single layer of SiO_2 particles was homogeneously distributed on the sample surface to measure the local strain distribution [40,41]. At each deformation stage, ROIs have been imaged using different SEM detectors, i.e., for SEs, back-scattered electrons (BSE) and in-lens SEs. Based on the in-lens SE images of the local ROIs covered with SiO_2 , the micro-DIC analysis was carried out using the ARAMIS software. After finishing 5 deformation steps, reaching a global average strain in horizontal loading direction ($\epsilon_{x\text{-avg}}$) of 20.8%, EBSD analysis was performed again for the same ROIs using a JEOL-JSM-6500F field emission SEM to reveal the TRIP effect.

3. Results

3.1. Microstructural characterization

The SE, EBSD and TEM results are shown in Fig. 1. The steel is composed of ferrite, martensite and retained austenite, where the ferrite fraction is about 40 vol %, as shown in Fig. 1(a). The EBSD and TEM results shown in Fig. 1(b)–(j) reveal that ultra-fine film-like retained austenite with a thickness range of about 20–150 nm mainly exists in the martensite regions far away from ferrite. The retained austenite films show a K–S orientation relationship with the adjacent martensite laths, as revealed by the selected area electron diffraction patterns shown in Fig. 1(f) and (h). Retained austenite located near the F/M interfaces exhibits a blocky morphology with a side length of about 300–600 nm, as shown in Fig. 1(i)–(j). From the IPF map and the grain boundary map, respectively, shown in Fig. 1(c) and (d), we observe that the grain boundaries among ferrite grains are mainly high angle grain boundaries with misorientations above 15° . Almost no orientation gradient exists within individual ferrite grains.

Fig. 2 shows the EDX analysis results of the distribution of Si, Mn and Al in the microstructure. Figs. 2(a) and Fig. 1(a) reveal banded structures consisting of ferrite and martensite bands which are aligned parallel to the rolling plane. Two factors may affect such banding, i.e., chemical segregation and shape changes during hot rolling [57,58]. Fig. 2 (b) shows that no obvious segregation of Si, Mn and Al exists among the bands. These results indicate that the banded microstructures do not result from chemical segregation but from grain shape changes induced by hot rolling.

3.2. Macro-DIC analysis and mechanical property

The macro-DIC analysis results are shown in Fig. 3. The von Mises strain maps reveal that the strain distribution on the sample surface is inhomogeneous in both, the uniform elongation stage and the necking stage. Fig. 3(a) shows the strain distribution when the average strain is $\epsilon_{x\text{-avg}} = 4.2\%$. Distinct strain localization regions almost cover the whole parallel section of the sample and mainly distributes along the 45° direction of the longitudinal axis. The local strain can reach up to 4.53% at a total deformation of $\epsilon_{x\text{-avg}} = 4.2\%$. The inhomogeneous distribution of the strain intensifies with increasing average strain. Fig. 3(b) shows the strain distribution just before fracture. It reveals that the highest local strain in the center of the necking region reaches a value up to about 67.0% at an average strain of $\epsilon_{x\text{-avg}} = 30.2\%$, while the local strain in the uniform elongation region remains mainly below 20.0%.

Based on the strain map shown in Fig. 3(b), the von Mises strain distribution along the central longitudinal section of the sample before fracture is obtained, as shown in Fig. 3(c). The strain values of the points in the left-half part with 0.5 mm, 1.0 mm, 1.5 mm, 2.0 mm, 2.5 mm and 3.0 mm away from the fracture top are, respectively, 58.2%, 36.9%, 23.0%, 17.6%, 13.3% and 9.6%. The engineering stress-strain curve obtained based on the macro-DIC strain measurement using the three-line method (the engineering strain is calculated based on the average strain of the three lines parallel to the long axis of the tensile sample within the gauge length range) is shown in Fig. 3(d). It reveals that the YS, UTS and elongation of the sample are 516 MPa, 949 MPa and 30.2%, respectively.

3.3. Characterization of the microstructure at different local strain

The XRD results of local regions of different strains are shown in Fig. 4. Fig. 4(a) shows the XRD profiles containing the fcc {111} peak. The decrease of the peak height reveals that retained austenite transformed with the increase of the local strain. Based on the fcc

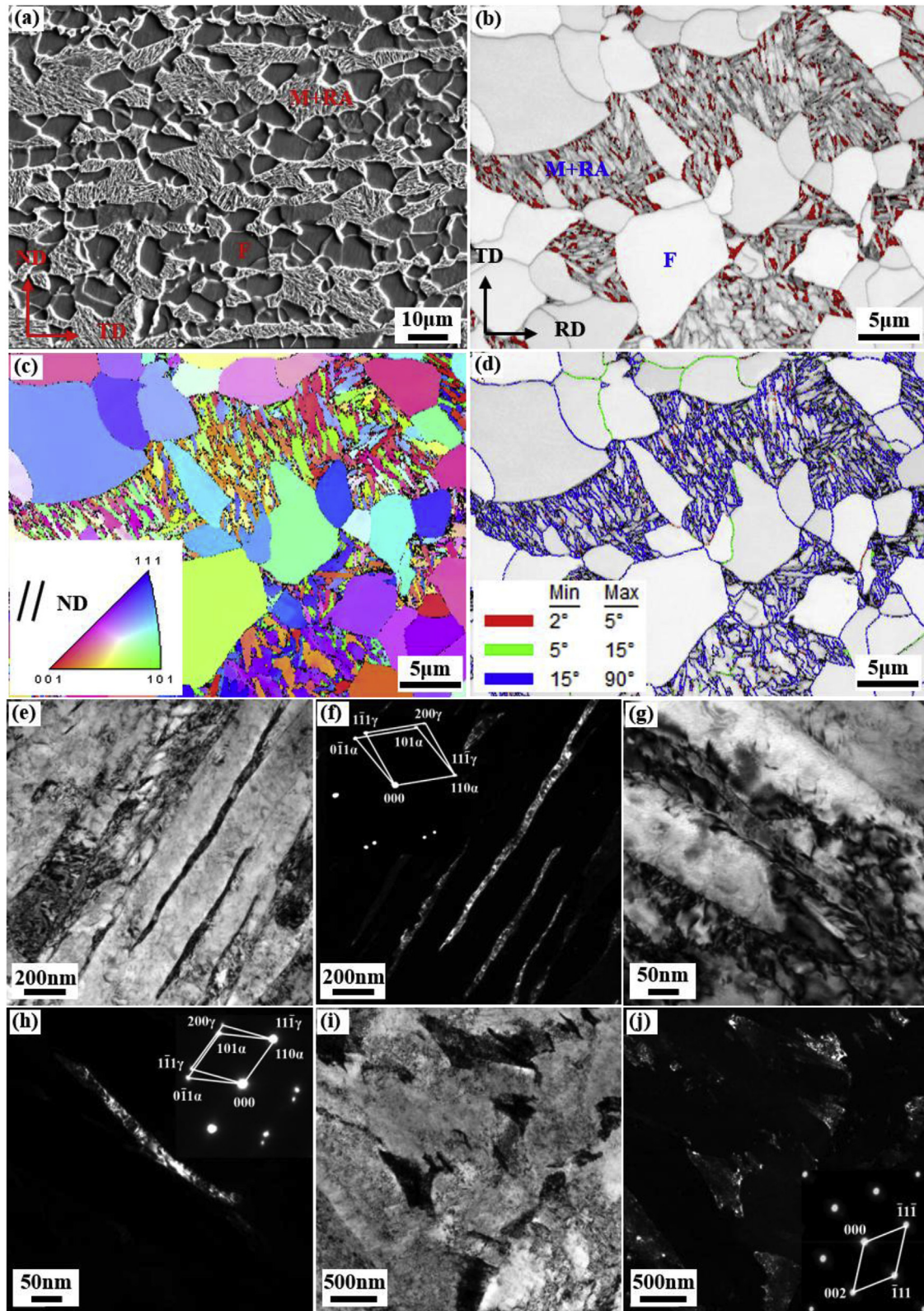


Fig. 1. Microstructures of the sample: (a) SE image; (b) EBSD image quality map with austenite in red; (c) IPF map; (d) image quality map with grain boundaries (grain boundaries with 2–5° misorientation in red, 5–15° misorientation in green, 15–90° misorientation in blue); (e) (g) bright field image for the retained austenite films; (f) (h) dark field image for the retained austenite films; (i) bright field image for the blocky retained austenite; (j) dark field image for the blocky retained austenite. “F”, “M” and “RA” are ferrite, martensite and retained austenite, respectively. (For interpretation of the references to color in this figure legend, the reader is referred to the Web version of this article.)

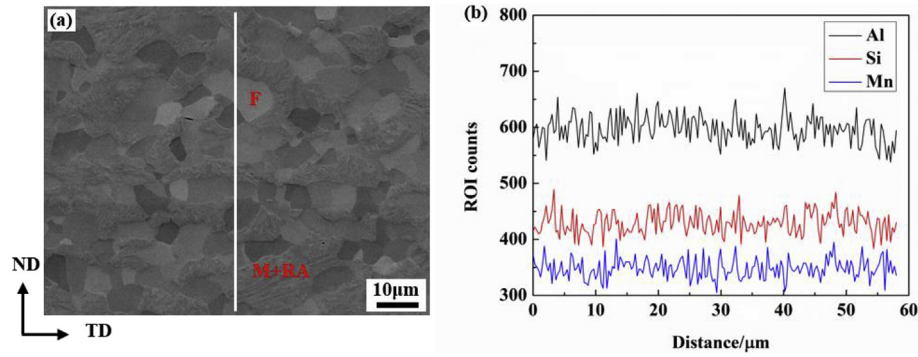


Fig. 2. EDX analysis results of the distribution of Si, Mn and Al: (a) SE image; (b) EDX line scanning results across different ferrite bands and martensite bands (white line in (a)). “F”, “M” and “RA” are ferrite, martensite and retained austenite, respectively.

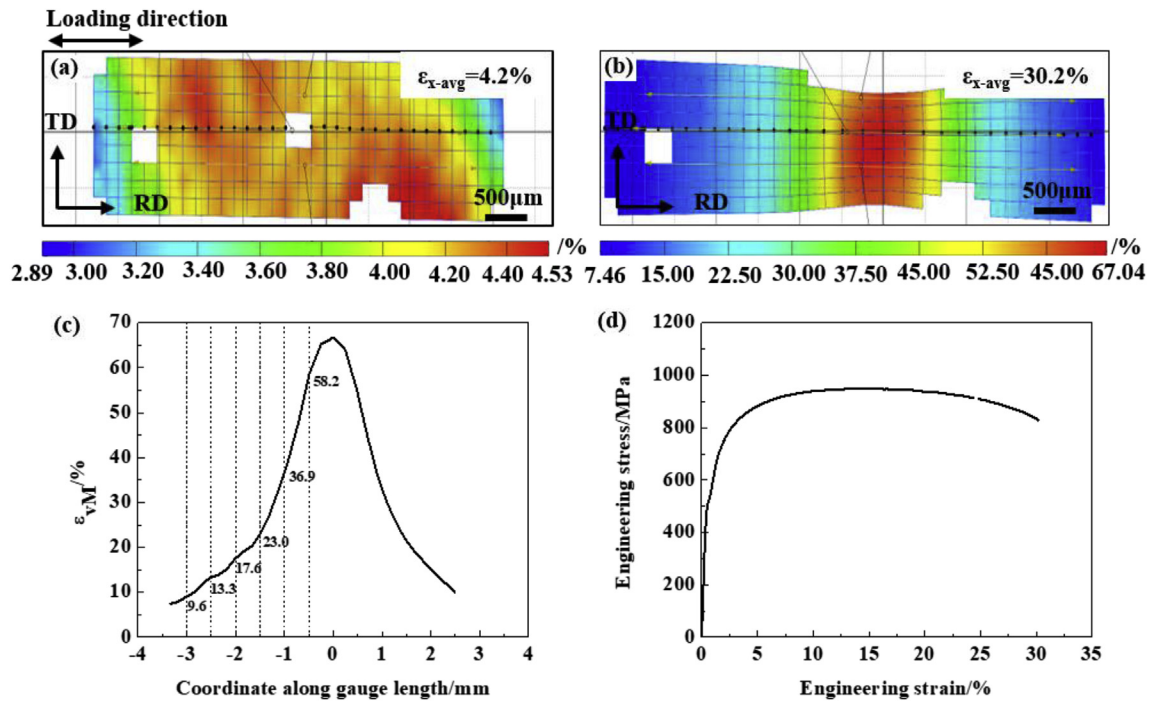


Fig. 3. Results of the uniaxial tensile test observed by using macro-DIC: (a) von Mises strain map along the sample surface at an average strain of $\epsilon_{x-avg} = 4.2\%$; (b) von Mises strain map along the sample surface taken at an average strain of $\epsilon_{x-avg} = 30.2\%$; (c) von Mises strain profile along the gauge length of the sample according to the middle solid line in Fig. 2(b); (d) engineering stress-strain curve. ϵ_{x-avg} is the global average strain in horizontal loading direction and ϵ_{vM} is the local von Mises strain.

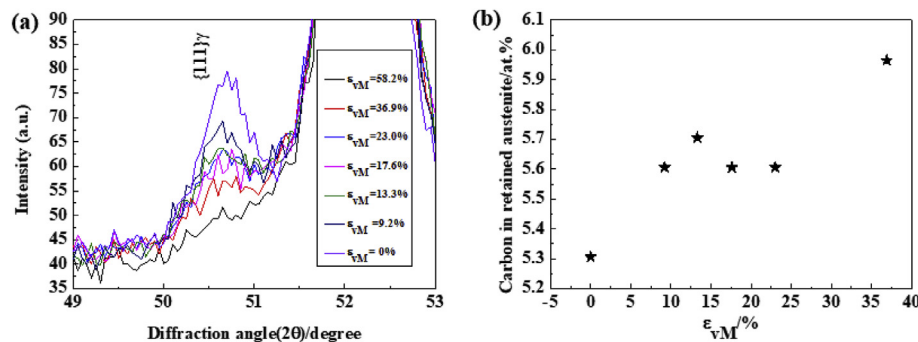


Fig. 4. XRD results taken at positions of different local strain along the rolling section of the fractured macro-DIC tensile sample: (a) XRD profiles containing the fcc {111} peak; (b) average carbon concentration of the retained austenite in the local regions as obtained by analysis of the XRD peak shift. ϵ_{vM} is the local von Mises strain. The carbon concentration is given in at. %.

{111} peak, the retained austenite carbon concentration was approximated and the corresponding results are shown in Fig. 4(b). A similar carbon concentration calculation method was used and documented elsewhere [7]. The retained austenite with a carbon concentration below 5.6 at. % has transformed into martensite at a local von Mises strain of 25.0%, while retained austenite with a carbon concentration above 6.0 at. % remains stable even after reaching a local von Mises strain of 36.9%. The respective values for the carbon content have been obtained by analysis of the XRD peak shift [37].

To investigate the fracture behavior of the ferrite-containing Q&P steel during tensile deformation, EBSD analysis was performed in local regions containing micro-cracks near the fracture region, at a local von Mises strain of $\varepsilon_{VM} = 58.2\%$, Fig. 5. The image quality map (Fig. 5(a)) shows that the micro-cracks mainly initiate at the intersections of two opposing ferrite regions and two opposing martensite regions and then propagate along the F/M interfaces. Fig. 5(a) also shows that retained austenite still exists in the local regions adjacent to the micro-cracks. This means that micro-cracks can initiate before all of the retained austenite is consumed by the TRIP effect. With an intersection angle of $30\text{--}40^\circ$, the micro-crack profile facing toward the F/M interface is much sharper than the inclined ones (with an intersection angle of $120\text{--}180^\circ$) facing toward martensite or ferrite regions, as revealed in the local enlarged image shown in Fig. 5(a). This specific

morphology of the micro-crack profiles promotes stress concentration and hence strain localization on the interfaces, leading to crack formation and propagation along them during deformation [42,43]. Obvious blunting of the crack tips occurs when the cracks propagate into the ferrite. This means that soft ferrite can indeed partly retard crack propagation [44]. The corresponding grain boundary map shown in Fig. 5(b) reveals that large numbers of low-angle grain boundaries ($2\text{--}15^\circ$) exist in regions near the micro-crack tips. Fig. 5(c) and (d) show the IPF maps of the ferrite, martensite and retained austenite. Substantial orientation spread and pronounced orientation substructures exist in the ferrite grains, especially in those located near the cracks. These observations suggest that strain localization indeed occurred in the crack initiation regions. Fig. 5(b) also shows that the fraction of low-angle grain boundaries in the ferrite is much higher than that in the martensite. This result indicates that strain is mainly partitioned in the ferrite during deformation. These results qualitatively show that the deformability difference (or strain partitioning) between the ferrite and martensite results in strain localization on the F/M interfaces, leading to crack initiation [37,41,44]. Thus, optimizing the strain partitioning between the soft phase and hard phase should be an effective way to improve the ductility.

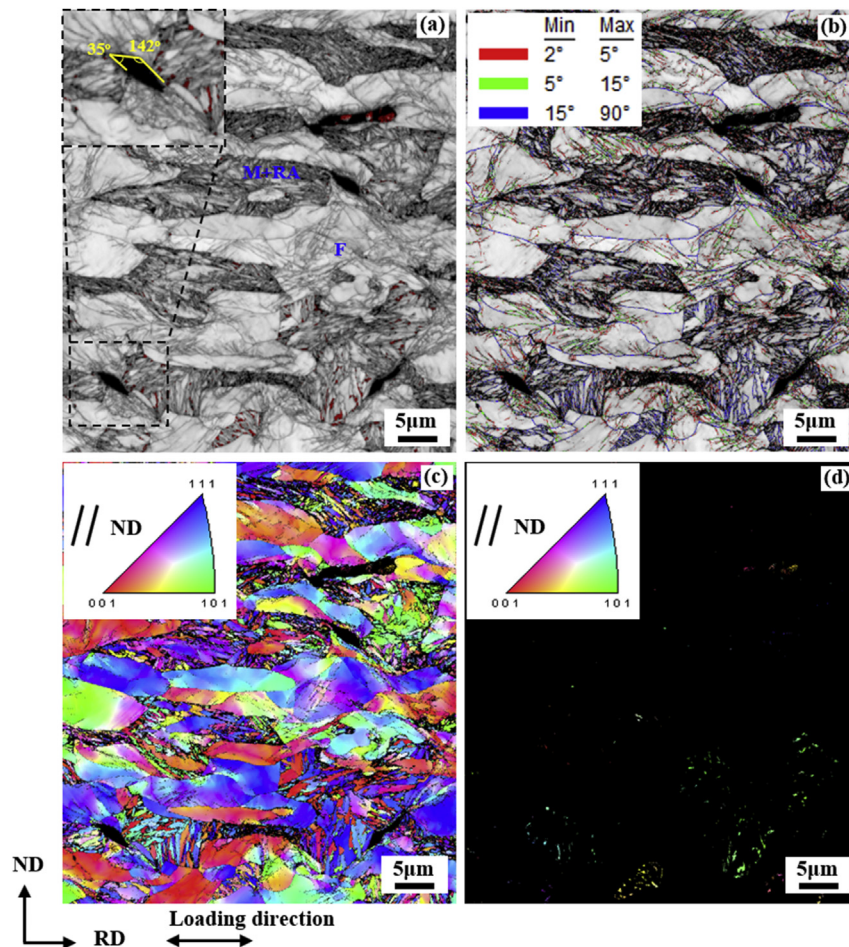


Fig. 5. EBSD results of the region containing micro-cracks near the fracture region, at a local von Mises strain of $\varepsilon_{VM} = 58.2\%$: (a) image quality map with retained austenite in red; (b) image quality map with grain boundaries (grain boundaries with $2\text{--}5^\circ$ misorientation in red, $5\text{--}15^\circ$ misorientation in green, $15\text{--}90^\circ$ misorientation in blue); (c) IPF map containing ferrite, martensite and retained austenite; (d) IPF map of the retained austenite. “F”, “M” and “RA” are ferrite, martensite and retained austenite, respectively. (For interpretation of the references to color in this figure legend, the reader is referred to the Web version of this article.)

3.4. Atom probe tomography analysis

The APT analysis results of the elemental partitioning among the phases are shown in Fig. 6. The retained austenite in Fig. 6(a) is the film-like retained austenite with a thickness of about 25 nm located inside the martensite region. The pink color represents the carbon atoms and green represents the iso-surface with a carbon atom fraction of 3.0 at. %. Fig. 6(b) shows the element distribution along the longitudinal axis of the ROI shown in Fig. 6(a). Fig. 6(b) shows that the carbon distribution across the retained austenite film is nonuniform and the carbon concentration is in the range 6.0–7.5 at. %. The carbon concentration in the retained austenite is much higher than that in the martensite (1.0–2.0 at. %) and an obvious carbon concentration gradient of up to 1.1 at. %/nm exists across the phase interface [59].

Fig. 6(c) shows the element distribution near the interface between martensite and the blocky retained austenite with a side length of about 300 nm located near the ferrite. Fig. 6(d) shows the element distribution curves along the long axis of the ROI cylinder shown in Fig. 6(c). Compared with the film-like retained austenite, the blocky retained austenite has lower carbon concentration of 4.0–6.0 at. %. The carbon concentration of the martensite is

0.5–1.0 at. %. Fig. 6(e) shows the APT analysis results of the ferrite and the element distribution curves along the long axis of the ROI cylinder are shown in Fig. 6(f). The elements distribute almost homogeneously in the ferrite. With a carbon concentration of 0.2–0.5 at. %, the ferrite contains much less carbon than the retained austenite and martensite. The APT analysis results of the retained austenite, martensite and ferrite reveal that the distribution of Si, Mn, Al and P in the phases are almost homogeneous and the corresponding concentrations are 1.0–2.0 at. %, 1.0–2.5 at. %, 3.0–5.0 at. % and 0.2 at. %, respectively.

The APT analysis of the carbides in the martensite is shown in Fig. 7. The green interfaces in Fig. 7(a) are carbon iso-concentration surfaces for a carbon concentration of 15.0 at. %. We observe that carbon enriched regions with rod-like morphology exist near the martensite/austenite interfaces. These regions with a carbon concentration ranging between 15.0 at. % and 30.0 at. % are likely carbides. Fig. 7(b) and (c) respectively reveal the element distribution curves across the 15.0 at. % C iso-surface of carbide 1 and carbide 2 shown in Fig. 7(a). The data show that the carbon concentration in the carbide is much higher than that in its adjacent matrix while no significant difference occurs for Si, Mn, Al and P. With a carbon concentration of about 25.0 at. % in the center, carbide 1 matches

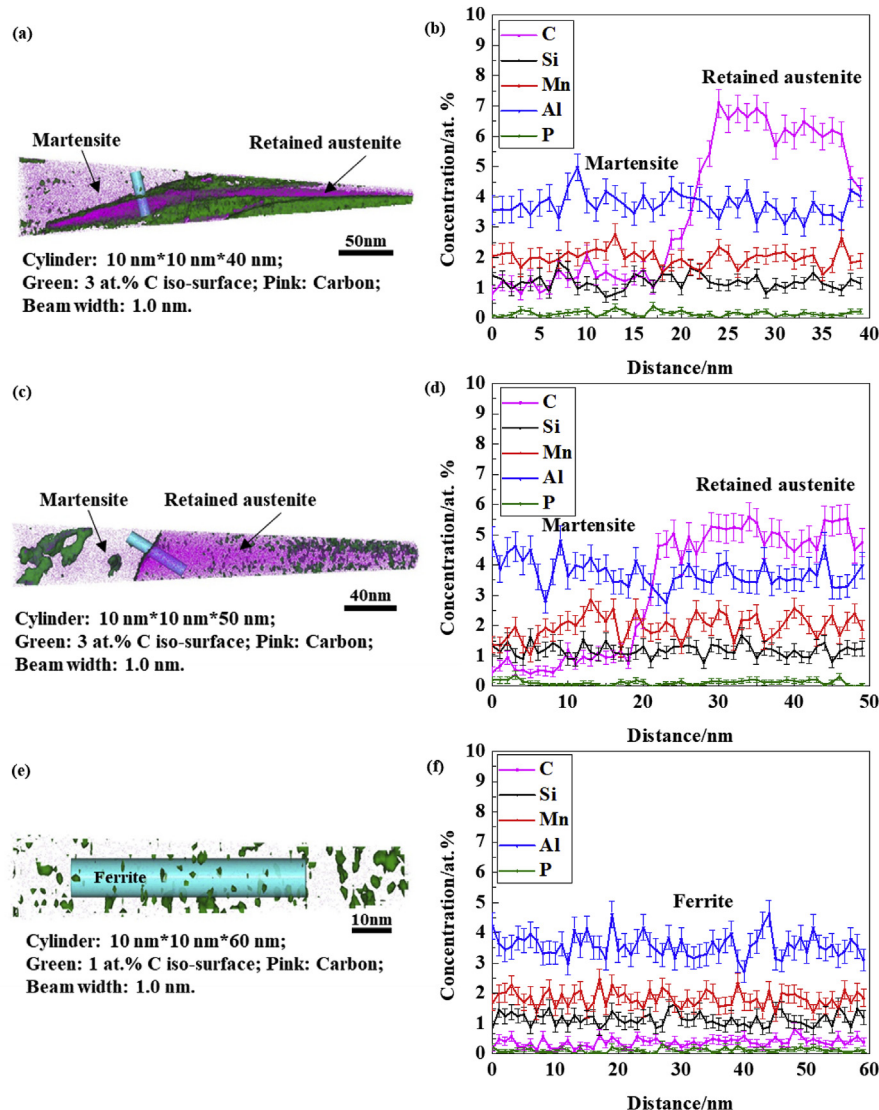


Fig. 6. APT analysis results of the elemental partitioning: (a) (b) martensite and film-like retained austenite; (c) (d) martensite and blocky retained austenite; (e) (f) ferrite. All concentrations are given in at. %.

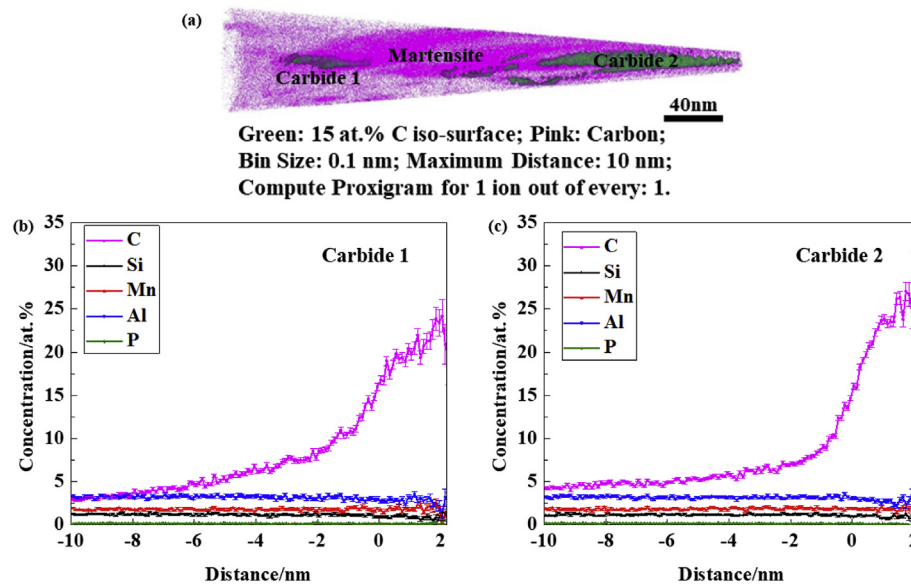


Fig. 7. APT analysis results of the carbides in the martensite: (a) rod-like carbides in martensite; (b) analysis results of carbide 1; (c) analysis results of carbide 2. All concentrations are given in at.%.

the stoichiometry of Fe_3C . For carbide 2, the carbon concentration in the center is about 30.0 at. %, thus, it approaches the stoichiometry of the $\text{Fe}_{2.4}\text{C}$ [60]. The existence of carbides in the martensite demonstrates that addition of 1.48 wt % Al cannot completely suppress carbide formation in the Q&P steel.

3.5. Quasi in-situ analysis of strain partitioning and TRIP effect

The EBSD results of the microstructure near the fracture top shown in Fig. 5(a) reveal that the retained austenite located in the small martensite regions with an average dimension (martensite island size) below $5\text{ }\mu\text{m}$ surrounded by ferrite grains is harder to transform during the deformation, compared with the retained austenite located in the large martensite regions with an average size above $10\text{ }\mu\text{m}$. This observation suggests that the F/M fraction ratio and the martensite morphology may have a significant effect on the strain partitioning between ferrite and martensite and thus influence the onset of the TRIP effect. According to the ferrite fraction and martensite morphology, two types of scenarios were observed: In type-1 regions, the ferrite fraction is lower or equal to the martensite fraction. The involved martensite region generally has a large size (martensite island size) above $10\text{ }\mu\text{m}$ and the F/M interface exhibits a concave polygon morphology. In type-2 regions, the ferrite fraction is higher than the martensite fraction. The size of the martensite region is below $5\text{ }\mu\text{m}$ and the F/M interface exhibits a convex polygon morphology.

These two types of morphology are mainly attributed to the inhomogeneous nucleation and growth of the ferrite grains resulting from the inhomogeneous deformation of the high temperature austenite grains. The size and morphology of the martensite region are controlled by the amount, size and morphology of its surrounding ferrite grains. For the local regions with lower ferrite fraction and smaller ferrite grain size, the martensite islands are more likely to exhibit a concave polygonal morphology and a larger size. On the contrary, for regions with larger ferrite fraction and larger ferrite grain size, the martensite islands are more likely to exhibit a convex polygonal morphology and a smaller size.

Fig. 8 shows a quantitative analysis of the strain contrast among

the different phases for the type-1 region. Fig. 8(a) shows the EBSD results of the analyzed region without deformation. Fig. 8(b) and (c) give the von Mises strain distribution of the region at an average strain of $\varepsilon_{x\text{-avg}} = 4.2\%$ and $\varepsilon_{x\text{-avg}} = 20.8\%$, respectively. Fig. 8(c) shows that the strain is concentrated at the intersections of two opposing ferrite regions and two opposing martensite regions. Strain localization exists at the inflection points on the F/M interface where the interface protrudes into the martensite regions. In such regions, strain localization bands can even penetrate into the martensite. Four lines were chosen to analyze the von Mises strain contrast among the different phases. Fig. 8(d) reveals the von Mises strain distribution along line 1 which passes through the ferrite grain 1 (F 1) and martensite region 1 (M + RA 1). We observe that an obvious strain contrast exists between F 1 and M + RA 1. This means that a strain gradient exists in such regions near the F/M interface [61,62]. The strain distribution along line 2 passing through M + RA 2 is shown in Fig. 8 (e). Strong strain localization exists in the martensite region. The highest local von Mises strain in M + RA 2 can reach up to 22.5% when the average strain is 20.8% and it exists on the strain localization band shown in Fig. 8 (c). Fig. 8(f) presents the von Mises strain distribution along line 3 crossing ferrite grain 2 (F 2) and the M + RA 1 region. It also reveals that a strong strain contrast exists between the ferrite grain and M + RA region. Comparison with Fig. 8(d) shows that the local strain in grain F 2 is much lower than that in F 1. Line 4 passes through the intersection of two opposing ferrite regions and two opposing martensite regions, where the highest local strain appears, as shown in Fig. 8(c). The strain distribution along line 4 shown in Fig. 8(g) reveals that the local von Mises strain at the intersection has reached up to 40.0% at an average strain of $\varepsilon_{x\text{-avg}} = 20.8\%$.

Fig. 9 shows the strain partitioning among the different phases and grains for the type-1 region. It can be seen that the local strain in ferrite is much higher than that in the martensite. Moreover, with increasing average strain, the local deformation of the ferrite proceeds much faster than that of the martensite [63]. Fig. 9(a) also shows that the strain inhomogeneities in both, ferrite and martensite increase with growing average strain. Compared with the martensite, the ferrite exhibits a much more pronounced strain

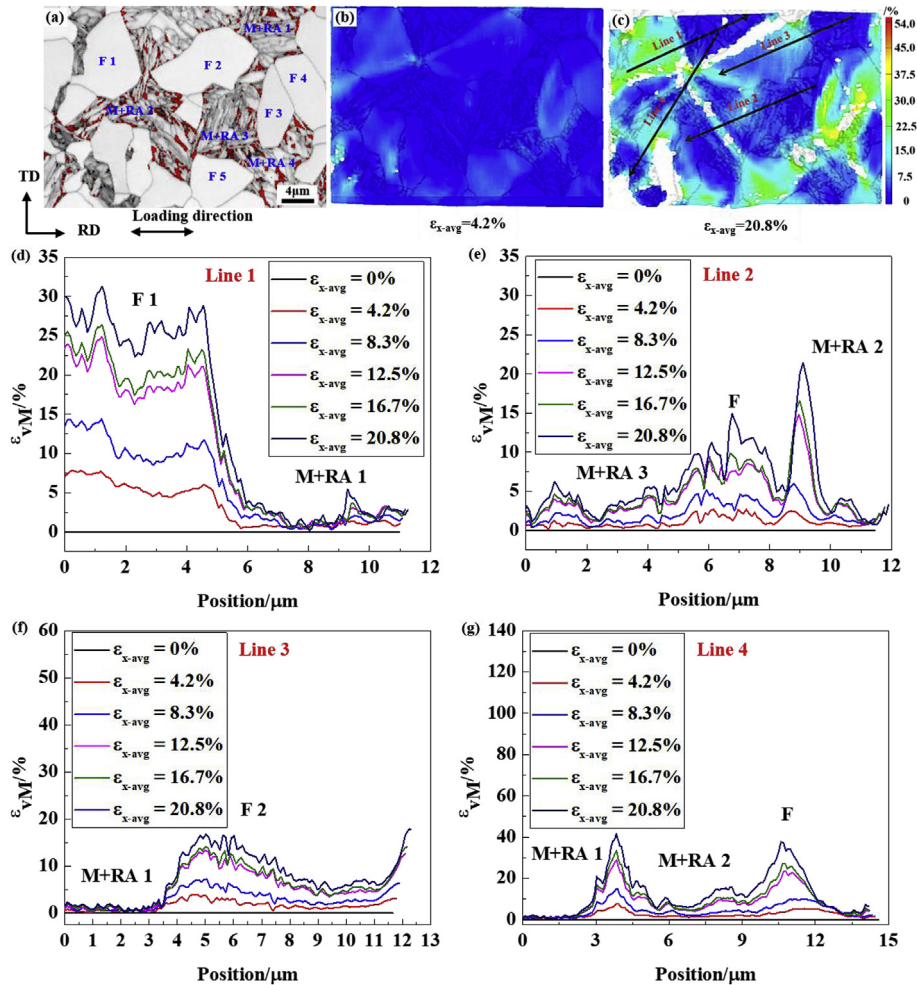


Fig. 8. Strain contrast among the different phases and grains in an exemplary type-1 region at different average strain: (a) EBSD results of the microstructure without deformation; (b) von Mises strain map of the local region with an average strain of $\varepsilon_{x-avg} = 4.2\%$ (indicated in the EBSD grain boundary map); (c) von Mises strain map of the local region at an average strain of $\varepsilon_{x-avg} = 20.8\%$ (indicated in the EBSD grain boundary map); (d) von Mises strain contrast along line 1; (e) von Mises strain contrast along line 2; (f) von Mises strain contrast along line 3; (g) von Mises strain contrast along line 4. ε_{x-avg} is the global average strain in horizontal loading direction and ε_{vM} is the local von Mises strain. “F”, “M” and “RA” are ferrite, martensite and retained austenite, respectively.

inhomogeneity. Fig. 9(b) shows the strain partitioning among the different ferrite grains. It can be seen that the individual ferrite grain which is surrounded by martensite (F 2) sustains the lowest local strain among the five ferrite grains. The ferrite grain with larger local strain possesses a larger strain inhomogeneity. Fig. 9(c) shows the strain partitioning among the different martensite regions. The martensite regions with different surrounding structures exhibit different local strain. The results also show that the strain inhomogeneity is much larger in the martensite region with larger local strain.

To investigate the local TRIP effect, EBSD analysis was again carried out on the region shown in Fig. 8 after 5 steps of deformation, Fig. 10. The image quality maps with the austenite in red, shown in Fig. 10(a)–(b), reveal that nearly 50% of the retained austenite located in martensite regions has undergone a TRIP effect when the average strain is $\varepsilon_{x-avg} = 20.8\%$. We find that the retained austenite located near the F/M interfaces is particularly prone to transform during loading. Retained austenite near the intersections of two opposing ferrite regions and two opposing martensite regions has entirely transformed at an average strain of 20.8%. The retained austenite orientation maps shown in Fig. 10(c)–(d) reveal that the orientations of the retained austenite grains are similar,

eliminating the possible influence of the retained austenite orientation on the TRIP effect. As the IPF maps shown in Fig. 10 (e)–(f) reveal, no significant orientation change has been observed in the martensite and retained austenite after tensile deformation. However, a pronounced orientation gradient exists in the ferrite grains, especially in those that have undergone substantial strain localization. Fig. 10(g)–(h) shows the Schmid factor map for the $\{110\} \langle 111 \rangle$ slip systems in the ferrite and martensite. The deformation results in orientation changes and an associated increase of the Schmid factor of ferrite grains with low initial Schmid factor (F1 and F5). In general, grains with larger Schmid factor deform at lower local stresses, thus promoting strain localization [64–66]. However, when considering both the strain map (Fig. 8(c)) and the Schmid factor map (Fig. 10(g)), we find that the ferrite grain 2 (F2) exhibits a much weaker strain localization than the ferrite grain 1 (F1), although it possesses a much larger initial Schmid factor. This is a result of the geometrical constraints imposed by the hard adjacent martensite. This topological constraint leads to a local load situation which substantially deviates from the macroscopic one [67].

Fig. 11 shows the strain contrast among the different phases for the type-2 region. Fig. 11(a) gives the EBSD results of the analyzed region prior to deformation. The strain distributions of the region

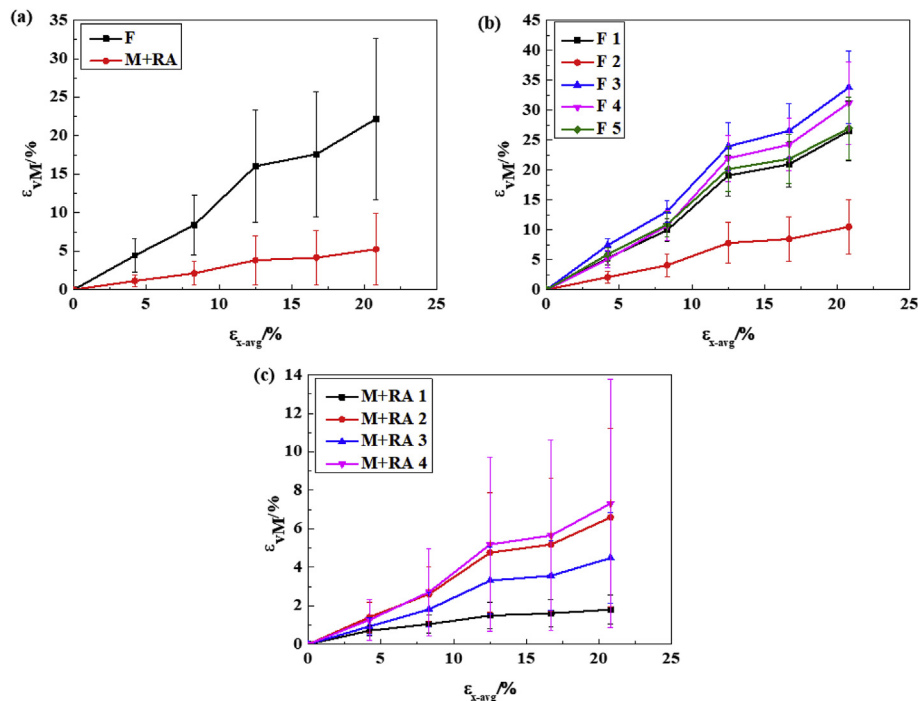


Fig. 9. Strain partitioning among the different phases and grains in an exemplary type-1 region at different average strain: (a) von Mises strain partitioning between ferrite and martensite; (b) von Mises strain partitioning among different ferrite grains; (c) von Mises strain partitioning among different martensite regions. ϵ_{x-avg} is the global average strain in horizontal loading direction and ϵ_{vM} is the local von Mises strain. “F”, “M” and “RA” are ferrite, martensite and retained austenite, respectively.

when the average strain is $\epsilon_{x-avg} = 4.2\%$ and $\epsilon_{x-avg} = 20.8\%$ are shown in Fig. 11(b) and (c), respectively. Fig. 11(c) reveals that the von Mises strain distribution in the large polygonal martensite region with an average dimension of about $10\ \mu\text{m}$ is inhomogeneous. Strain localization inside the martensite builds up approximately parallel to the martensite laths [49,59]. Different from the strain distribution in the large martensite region, no obvious non-uniform strain distribution exists in the small blocky martensite region (with average dimension below $5\ \mu\text{m}$) surrounded by ferrite. This zone experiences near-zero local strain. Two lines were selected to analyze the von Mises strain contrast among the different phases. Fig. 11(d) shows the von Mises strain distribution along line 1 crossing F 1 and M + RA 1. A strong strain contrast with a strain difference of about 45% exists between ferrite and martensite at an average strain of $\epsilon_{x-avg} = 20.8\%$. The strain distribution along line 2 is shown in Fig. 11(e). With the strain difference reaching up to about 50%, the strain contrast between F 1 and M + RA 2 is much larger than that between F 2 and M + RA 2 at an average strain of $\epsilon_{x-avg} = 20.8\%$.

Fig. 12 shows the quantitative analysis results of the von Mises strain partitioning among the different phases and grains in the type-2 region. The strain partitioning between ferrite and martensite is shown in Fig. 12(a). Comparing these data with the results shown in Fig. 9(a), we find that the increase of the ferrite fraction can lead to an obvious increase of strain inhomogeneity and to a slight increase of the local strain inside the ferrite. It also results in a significant decrease of the local strain and strain inhomogeneity in the martensite region. Fig. 12(b) reveals the strain partitioning among the ferrite grains. The local strain and strain inhomogeneity in individual ferrite grains surrounded by martensite regions (F 2) are much lower than those in ferrite grains pertaining to interconnected ferrite regions (F 1). The strain partitioning among the different martensite regions is shown in Fig. 12(c). Small martensite regions with average dimension $<5\ \mu\text{m}$ (M + RA 2) surrounded by ferrite exhibit lower local strain

and lower strain inhomogeneity than large martensite with dimensions of about $10\ \mu\text{m}$ (M + RA 1).

Fig. 13 shows the EBSD analysis results of the type-2 region. Fig. 13(a)–(b) reveals that the retained austenite located in the large martensite region with an average dimension of about $10\ \mu\text{m}$ performs a more pronounced TRIP effect than that located in the small martensite region with an average dimension below $5\ \mu\text{m}$. For the large martensite region, the majority of the blocky retained austenite grains distributed near the F/M interfaces transform into martensite upon tensile loading. The retained austenite grains located near the martensite region center also partly undergo a TRIP effect. For the small martensite region surrounded by ferrite, only the blocky retained austenite near the F/M interfaces has transformed. The retained austenite orientation maps shown in Fig. 13(c)–(d) reveal that the retained austenite grains in one martensite region have similar orientations. No specific preferred orientations were observed for those retained austenite grains that have undergone a TRIP effect. The IPF maps shown in Fig. 13(e)–(f) also reveal that the tensile deformation leads to orientation changes in the ferrite grains, especially in those that have undergone substantial strain localization. We also observed an increase of the Schmid factor in the ferrite grains with relatively low initial Schmid factor, as shown in Fig. 13(g)–(h).

4. Discussion

4.1. Relation among carbon partitioning, strain partitioning and TRIP effect

The essence of Q&P and TRIP steel design is to control the carbon partitioning behavior. It determines the phase transformation and influences the component, size, morphology and distribution of the phases [25,68,69]. For conventional martensite/retained austenite dual-phase Q&P steel, carbon mainly partitions between the initial martensite and untransformed austenite. However, in ferrite-

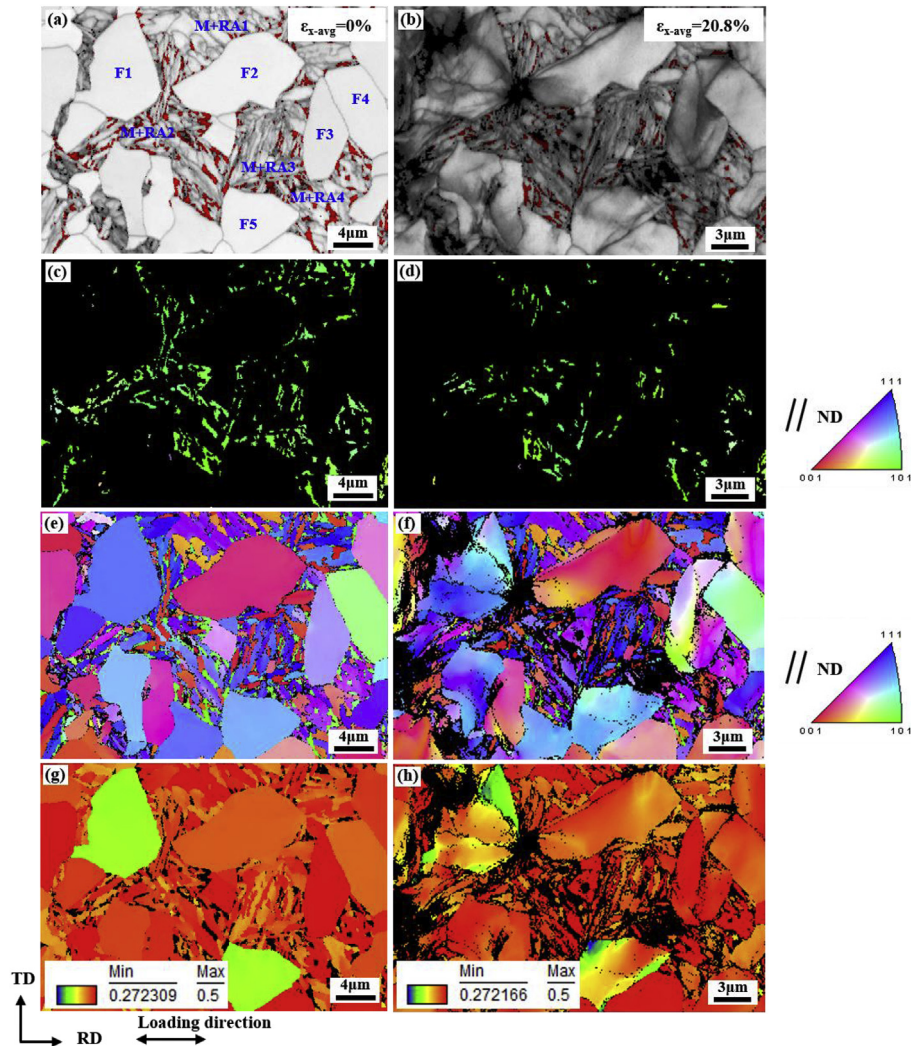


Fig. 10. EBSD analysis results of the type-1 region: (a) (b) Image quality map containing retained austenite (in red); (c) (d) IPF map of the retained austenite; (e) (f) IPF map containing ferrite, martensite and retained austenite; (g) (h) Schmid factor map for the $[110]\langle 111 \rangle$ slip systems in the ferrite and martensite; (a) (c) (e) (g) $\varepsilon_{x-avg} = 0\%$; (b) (d) (f) (h) $\varepsilon_{x-avg} = 20.8\%$. ε_{x-avg} is the global average strain in horizontal loading direction. “F”, “M” and “RA” are ferrite, martensite and retained austenite, respectively. (For interpretation of the references to color in this figure legend, the reader is referred to the Web version of this article.)

containing Q&P steel, carbon partitioning consists of two processes, i.e., partitioning between ferrite and high-temperature austenite (austenite in the intercritical two-phase region) and between initial martensite and untransformed austenite [37].

As the APT results (Fig. 6) reveal, the carbon concentration in the ferrite is 2–10 times lower than that in the martensite. Since the martensite forms from the high-temperature austenite, the carbon concentration of the martensite (0.5–2.0 at. %) reflects the carbon concentration of the preceding high-temperature intercritical austenite. The existence of more retained austenite in the local martensite regions near the F/M interfaces (as shown in Fig. 1(b)) demonstrates that a carbon concentration gradient exists inside the high-temperature austenite, characterized by higher carbon concentration in near-interface regions. This gradient stems from carbon partitioning and the associated transport gradients during ferrite formation. The higher carbon concentration in the austenite regions near the F/M interfaces promotes the formation of blocky retained austenite. In addition, the possible higher hydrostatic pressure on the untransformed austenite located near the F/M interfaces, caused by the volume expansion from the adjacent martensite transformation, can also promote formation of blocky

retained austenite. The carbon partitioning between the initial martensite and untransformed austenite determines the final carbon concentration and thermal stability of the retained austenite. As shown in Fig. 6, the film-like retained austenite exhibits 1.5–2.0 at. % higher carbon concentration than the blocky retained austenite. This is mainly attributed to its larger specific surface area and the shorter diffusion distance to be overcome during partitioning [37].

The amount and mechanical stability of the retained austenite are the two most important factors determining the TRIP effect. The primary task for Q&P steel design is to increase the retained austenite fraction and optimize the mechanical stability, and thus to improve the TRIP effect. Previous studies indicate that the mechanical stability of retained austenite is controlled by five factors, i.e., carbon concentration, size, morphology, orientation and stress state [51,70–73]. More precisely, the retained austenite with higher carbon concentration, smaller size and higher hydrostatic pressure exhibits higher mechanical stability [13,74–76]. Blocky retained austenite possesses lower mechanical stability than film-like retained austenite [77]. Retained austenite with normal direction of the $\{200\}$ planes perpendicular or parallel to the loading

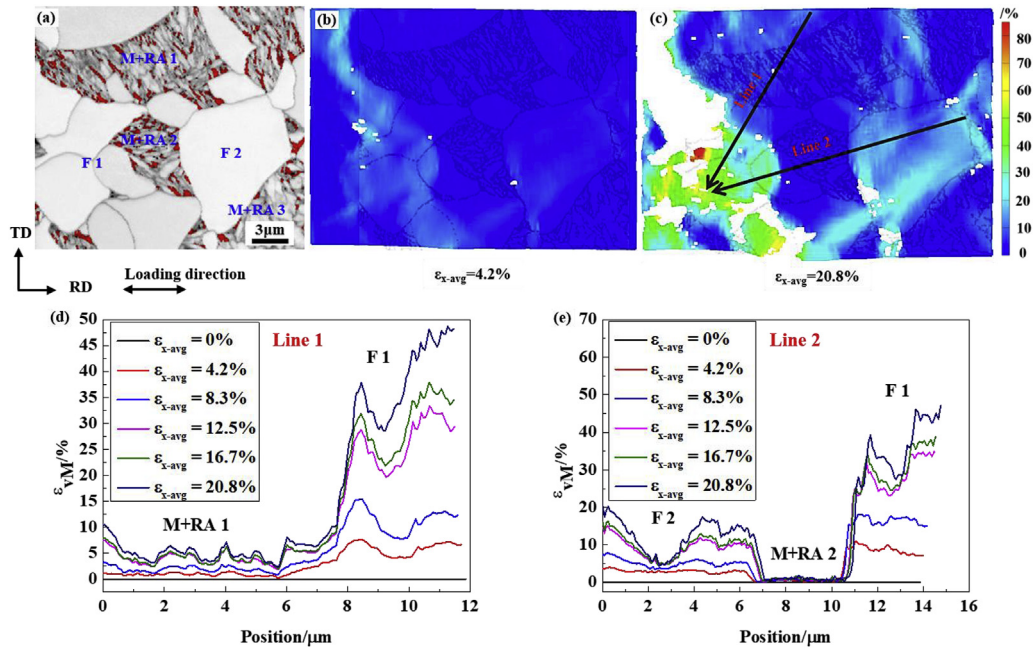


Fig. 11. Strain contrast among the different phases and grains in an exemplary type-2 region at different average strain: (a) EBSD results of the microstructure without deformation; (b) von Mises strain map of the local region with the average strain of $\epsilon_{x-avg} = 4.2\%$ (indicated in the EBSD grain boundary map); (c) von Mises strain map of the local region with the average strain of $\epsilon_{x-avg} = 20.8\%$ (indicated in the EBSD grain boundary map); (d) von Mises strain contrast along line 1; (e) von Mises strain contrast along line 2. ϵ_{x-avg} is the global average strain in horizontal loading direction and ϵ_{VM} is the local von Mises strain. “F”, “M” and “RA” are ferrite, martensite and retained austenite, respectively.

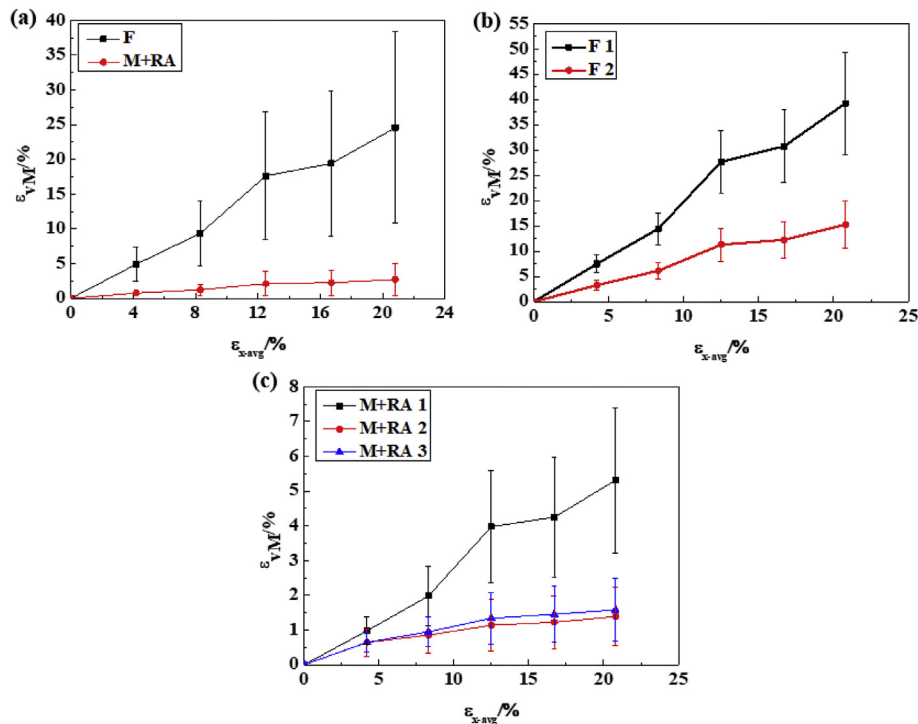


Fig. 12. Strain partitioning among the different phases and grains in an exemplary type-2 region at different average strain: (a) von Mises strain partitioning between ferrite and martensite; (b) von Mises strain partitioning among different ferrite grains; (c) von Mises strain partitioning among different martensite regions. ϵ_{x-avg} is the global average strain in horizontal loading direction and ϵ_{VM} is the local von Mises strain. “F”, “M” and “RA” are ferrite, martensite and retained austenite, respectively.

direction transform already at lower global deformation [78]. In fact, the local strain state of the surrounding phases should also have a significant effect on the mechanical stability of retained austenite, as retained austenite requires a certain strain level to

undergo a TRIP effect. Thus, ranking the austenite stability against deformation induced martensitic transformation by the average strain at the point of transformation might lead to misinterpretations in case of pronounced strain partitioning or strain

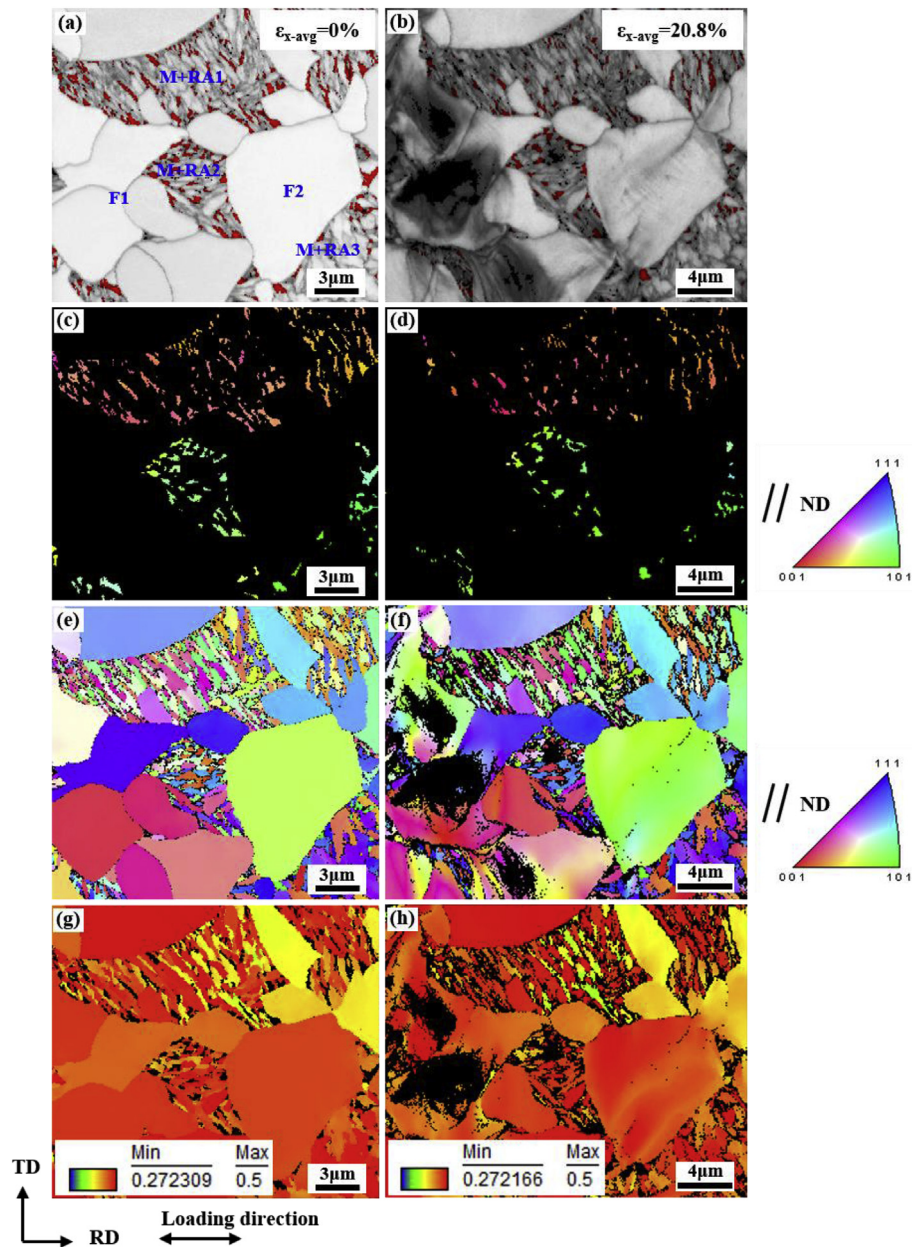


Fig. 13. EBSD analysis results of the type-2 region: (a) (b) Image quality map containing retained austenite (in red); (c) (d) IPF map of the retained austenite; (e) (f) IPF map containing ferrite, martensite and retained austenite; (g) (h) Schmid factor map for the $\{110\}\langle 111 \rangle$ slip systems in the ferrite and martensite; (a) (c) (e) (g) $\varepsilon_{x-avg} = 0\%$; (b) (d) (f) (h) $\varepsilon_{x-avg} = 20.8\%$. ε_{x-avg} is the global average strain in horizontal loading direction. "F", "M" and "RA" are ferrite, martensite and retained austenite, respectively. (For interpretation of the references to color in this figure legend, the reader is referred to the Web version of this article.)

localization effects which can profoundly alter the local micro-mechanical states relative to the macro-mechanical ones. In this case the local strain of the austenite region should be used to characterize its mechanical stability.

For Q&P steel containing ferrite, the retained austenite grains are mainly located inside the martensite region, thus the local strain in the martensite is an important factor controlling the TRIP effect. The local strain in the martensite depends on the average strain and the strain partitioning between ferrite and martensite. The micro-DIC results show that ferrite deforms earlier and stronger than martensite and the strain mainly localizes in the ferrite over the whole deformation process. This special strain partitioning with strong strain contrast at the F/M interfaces and low strain inside the martensite reduces the load exerted on the

austenite and thus reduces its TRIP response. In other words, the soft and compliant ferrite carries and accommodates the load that should ideally be better shared with the austenite to promote its gradual transformation. The strain contrast between ferrite and martensite is derived from their strength difference, which in turn mainly results from the difference in carbon concentration and the complex substructure hierarchy in the martensite.

For the ferrite-containing Q&P steel, the majority of the retained austenite exhibits a film-like morphology. Thus, the key for enhancing ductility lies in exploiting the austenite's size dependent transformation response, viz, forcing more of the film-like retained austenite to undergo a TRIP effect. Since most of the retained austenite films are located in martensite regions far away from the F/M interfaces, a key design task lies in increasing the local strain

inside the martensite and decrease the strain contrast between ferrite and martensite. This effect would homogenize the deformation, exerting less load on the ferrite and higher load on the austenite, triggering a very efficient TRIP effect in its confined film-like arrangement.

4.2. Microstructure design strategy for strength-ductility improvement

The micro-DIC analysis results show that the F/M fraction ratio, the martensite morphology and martensite size are important factors affecting strain partitioning among ferrite and martensite. In stiff regions with high martensite volume fraction above 50 vol%, less deformation work is used to deform the soft ferrite phase, hence more load is imposed on the austenite, enhancing the TRIP effect. This scenario can be explained in terms of two effects: First, the ferrite grains are divided into individual isolated zones by the percolating martensite when its fraction is above 50 vol %. Thus, the stiff martensite matrix acts as a hard cage and carries the majority of the load at the early deformation stage, delaying load sharing to the ferrite and retarding the build-up of high strain contrast at the F/M interfaces. The associated stress localization inside the martensite promotes the TRIP effect, even for the case of such small film-like austenite morphologies. Second, a smaller ferrite fraction leads for thermodynamic reasons to an increase of the high-temperature intercritically formed austenite fraction and a decrease of its carbon content. Austenite with lower carbon content transforms during cooling from the intercritical regime into martensite with lower strength. This effect decreases the strength difference between ferrite and martensite and thus also the strain contrast at the F/M interfaces. A more homogeneous deformation among the two regions promotes higher load sharing on the thin-film austenite, promoting the TRIP effect.

In the current alloy, martensite with dimensions (martensite island size) above 10 μm experiences higher deformation than martensite sized below 5 μm . This means that an appropriate increase of the martensite size promotes higher deformation of the martensite, thus promoting the TRIP effect. This phenomenon is attributed to the lower carbon content of martensite with larger size. As the micro-DIC results show, the concave polygon morphology of the martensite regions can promote formation of strain localization phenomena and increase the strain inside the martensite. Thus, the retained austenite located near the center of the martensite region readily performs a TRIP effect when being loaded. However, the large strains at the strain localization bands inside the martensite, exceeding even the strain in the ferrite, can also lead to cracks. Although the strain in the martensite region with convex polygon morphology is lower than that in its similar-sized martensite region with concave polygon morphology, strain localization parallel to the martensite laths is also beneficial for promoting the TRIP effect.

This analysis suggests that the design ferrite-containing Q&P steel should aim at the following microstructure features, namely, (i) a martensite fraction above 50 vol %; (ii) well isolated and non-percolating ferrite regions; (iii) martensite size above 5 μm ; and (iv) martensite regions with convex polygonal morphology.

The strain distribution results show that the local strain in the martensite region is still lower than that in the ferrite region, although the retained austenite inside the martensite region has undergone a TRIP effect. This means that the TRIP effect is not the main origin for the ductility of the current material. However, the TRIP effect, especially the TRIP effect of the retained austenite near F/M interfaces, can effectively reduce strain gradients near the interfaces. In other words, the TRIP effect in these regions partly relieves strain localization near the interfaces, thus buffering strain

contrast and attenuating local micromechanics for more compatible deformation between ferrite and martensite. Since the main reason for the ductility of ferrite-containing Q&P steel is the deformation of the soft ferrite phase, the main criterion for ductility improvement lies in delaying crack initiation at the F/M interfaces and utilizing the full deformation potential of the compliant ferrite. An appropriate decrease of the ferrite fraction and coarsening of the convex shaped martensite can effectively reduce the strain contrast at the F/M interfaces and increase the local strain carried by the martensite, thus also promoting the TRIP effect. In addition, a decrease of the strength difference between the ferrite and martensite by adjusting their precipitation state and/or introducing additional microstructure features, such as bainite, may also improve their compatible deformation capability and delay crack initiation, thus optimizing the strength-ductility combination of the steel further.

5. Conclusions

In this paper, a HDQ&P process was applied to a low-C low-Si Al-added steel and ferrite was introduced into the steel. The macro strain distribution across the sample surface and the micro strain distribution among the different phases were investigated by means of macro-DIC analysis and micro-DIC analysis combined with quasi in-situ tensile testing. The characterization of the carbon distribution among the different phases was carried out using APT. EBSD analysis was performed on different types of representative microstructure regions at different deformation stages during quasi in-situ tensile testing. By combining DIC, APT and EBSD, we investigated the relation among carbon partitioning, strain partitioning and mechanical properties in this ferrite-containing Q&P steel. The main results and conclusions are:

- (1) The carbon distribution in both martensite and retained austenite are inhomogeneous and strong carbon concentration gradients of up to 1.1 at. %/nm exists near the martensite/retained austenite interfaces. The blocky retained austenite near the F/M interfaces exhibits 1.5–2.0 at. % lower carbon concentration compared with the retained austenite films located near the martensite center regions.
- (2) The TRIP effect in the ferrite-containing Q&P steel mainly results from the special strain partitioning state between the ferrite and martensite, especially low local strains in the martensite region.
- (3) A decrease in the ferrite fraction and promotion of both, coarsening of the martensite and its polygonization can effectively enhance local deformation inside the martensite regions, promoting the TRIP effect.
- (4) The main origin for ductility of the ferrite-containing Q&P steel is the ferrite deformation. The key for the ductility improvement is to delay the crack initiation on the F/M interface and then make full use of the compliant deformation potential of the ferrite.
- (5) To achieve corresponding strength-ductility improvements, ferrite-containing Q&P steel should aim at the following microstructure features, namely, (i) a martensite fraction above 50 vol %; (ii) well isolated and non-percolating ferrite regions; (iii) martensite size above 5 μm ; and (iv) martensite regions with convex polygon morphology.

Acknowledgments

The authors are grateful to the kind support from the Chongqing Research Program of Basic Research and Frontier Technology (No. cstc2018jcyjAX0221), the Start-up Grant from Southwest

University (Grant No. SWU117054) and the State Scholarship Fund of Chinese Scholarship Council (CSC) (No. 201506080070). The authors would like to thank Mr. Huansheng He and Ms. Jun Yan (from Southwest University) for their help in analyzing the EBSD data and the microstructure formation mechanisms.

References

- [1] T. Tsuchiyama, J. Tobata, T. Tao, N. Nakada, S. Takaki, Quenching and partitioning treatment of a low-carbon martensitic stainless steel, *Mater. Sci. Eng., A* 532 (2012) 585–592.
- [2] D. De Knijf, R. Petrov, C. Foejer, L.A.I. Kestens, Effect of fresh martensite on the stability of retained austenite in quenching and partitioning steel, *Mater. Sci. Eng., A* 615 (2014) 107–115.
- [3] X.D. Wang, Z.H. Guo, Y.H. Rong, Mechanism exploration of an ultrahigh strength steel by quenching-partitioning-tempering process, *Mater. Sci. Eng., A* 529 (2011) 35–40.
- [4] J. Speer, D.K. Matlock, B.C. De Cooman, J.G. Schroth, Carbon partitioning into austenite after martensite transformation, *Acta Mater.* 51 (2003) 2611–2622.
- [5] J.G. Speer, D.V. Edmonds, F.C. Rizzo, D.K. Matlock, Partitioning of carbon from supersaturated plates of ferrite, with application to steel processing and fundamentals of the bainite transformation, *Curr. Opin. Solid State Mater. Sci.* 8 (2004) 219–237.
- [6] D.V. Edmonds, K. He, F.C. Rizzo, B.C. De Cooman, D.K. Matlock, J.G. Speer, Quenching and partitioning martensite - a novel steel heat treatment, *Mater. Sci. Eng., A* 438 (2006) 25–34.
- [7] X. Tan, Y. Xu, X. Yang, D. Wu, Microstructure-properties relationship in a one-step quenched and partitioned steel, *Mater. Sci. Eng., A* 589 (2014) 101–111.
- [8] X. Tan, Y. Xu, X. Yang, Z. Liu, D. Wu, Effect of partitioning procedure on microstructure and mechanical properties of a hot-rolled directly quenched and partitioned steel, *Mater. Sci. Eng., A* 594 (2014) 149–160.
- [9] J. Mola, B.C. De Cooman, Quenching and partitioning (Q&P) processing of martensitic stainless steels, *Metall. Mater. Trans. A* 44A (2013) 946–967.
- [10] H.Y. Li, X.W. Lu, W.J. Li, X.J. Jin, Microstructure and mechanical properties of an ultrahigh-strength 40SiMnNiCr steel during the one-step quenching and partitioning process, *Metall. Mater. Trans. A* 41A (2010) 1284–1300.
- [11] E. De Moor, S. Lacroix, A.J. Clarke, J. Penning, J.G. Speer, Effect of retained austenite stabilized via quench and partitioning on the strain hardening of martensitic steels, *Metall. Mater. Trans. A* 39A (2008) 2586–2595.
- [12] M.J. Santofimia, L. Zhao, R. Petrov, J. Sietsma, Characterization of the microstructure obtained by the quenching and partitioning process in a low-carbon steel, *Mater. Char.* 59 (2008) 1758–1764.
- [13] A.J. Clarke, J.G. Speer, M.K. Miller, R.E. Hackenberg, D.V. Edmonds, D.K. Matlock, F.C. Rizzo, K.D. Clarke, E. De Moor, Carbon partitioning to austenite from martensite or bainite during the quench and partition (Q&P) process: a critical assessment, *Acta Mater.* 56 (2008) 16–22.
- [14] J. Mola, B.C. De Cooman, Quenching and partitioning processing of transformable ferritic stainless steels, *Scripta Mater.* 65 (2011) 834–837.
- [15] S. Zhou, K. Zhang, Y. Wang, J.F. Gu, Y.H. Rong, High strength-elongation product of Nb-microalloyed low-carbon steel by a novel quenching-partitioning-tempering process, *Mater. Sci. Eng., A* 528 (2011) 8006–8012.
- [16] A.J. Clarke, J.G. Speer, D.K. Matlock, F.C. Rizzo, D.V. Edmonds, M.J. Santofimia, Influence of carbon partitioning kinetics on final austenite fraction during quenching and partitioning, *Scripta Mater.* 61 (2009) 149–152.
- [17] N. Zhong, X. Wang, Y. Rong, L. Wang, Interface migration between martensite and austenite during quenching and partitioning (Q&P) process, *J. Mater. Sci. Technol.* 22 (2006) 751–754.
- [18] J.G. Speer, E. De Moor, A.J. Clarke, Critical assessment 7: quenching and partitioning, *Mater. Sci. Technol. Lond* 31 (2015) 3–9.
- [19] F. Tariq, R.A. Baloch, One-step quenching and partitioning heat treatment of medium carbon low alloy steel, *J. Mater. Eng. Perform.* 23 (2014) 1726–1739.
- [20] J. Kaehkoenen, D.T. Pierce, J.G. Speer, E. De Moor, G.A. Thomas, D. Coughlin, K. Clarke, A. Clarke, Quenched and partitioned CMnSi steels containing 0.3 wt.% and 0.4 wt.% carbon, *Jom-Us* 68 (2016) 210–214.
- [21] B.C. De Cooman, S.J. Lee, S. Shin, E.J. Seo, J.G. Speer, Combined intercritical annealing and Q&P processing of medium Mn steel, *Metall. Mater. Trans. A* 48A (2017) 39–45.
- [22] J. Kang, C. Wang, Y. Li, G. Yuan, G. Wang, Effect of direct quenching and partitioning treatment on mechanical properties of a hot rolled strip steel, *J. Wuhan Univ. Technol.* 31 (2016) 178–185.
- [23] M.J. Santofimia, J.G. Speer, A.J. Clarke, L. Zhao, J. Sietsma, Influence of interface mobility on the evolution of austenite-martensite grain assemblies during annealing, *Acta Mater.* 57 (2009) 4548–4557.
- [24] M.J. Santofimia, L. Zhao, J. Sietsma, Model for the interaction between interface migration and carbon diffusion during annealing of martensite-austenite microstructures in steels, *Scripta Mater.* 59 (2008) 159–162.
- [25] X. Tan, Y. Xu, X. Yang, Z. Hu, F. Peng, X. Ju, D. Wu, Austenite stabilization and high strength-elongation product of a low silicon aluminum-free hot-rolled directly quenched and dynamically partitioned steel, *Mater. Char.* 104 (2015) 23–30.
- [26] Y. Toji, G. Miyamoto, D. Raabe, Carbon partitioning during quenching and partitioning heat treatment accompanied by carbide precipitation, *Acta Mater.* 86 (2015) 137–147.
- [27] E.J. Seo, L. Cho, B.C. De Cooman, Modified methodology for the quench temperature selection in quenching and partitioning (Q&P) processing of steels, *Metall. Mater. Trans. A* 47A (2016) 3797–3802.
- [28] H. Zhao, W. Li, L. Wang, S. Zhou, X. Jin, The deformation behavior analysis and mechanical modeling of step/intercritical quenching and partitioning-treated multiphase steels, *Metall. Mater. Trans. A* 47A (2016) 3943–3955.
- [29] S. Qin, Y. Liu, Q. Hao, Y. Wang, N. Chen, X. Zuo, Y. Rong, The mechanism of high ductility for novel high-carbon quenching-partitioning-tempering martensitic steel, *Metall. Mater. Trans. A* 46A (2015) 4047–4055.
- [30] H.L. Yi, P. Chen, Z.Y. Hou, N. Hong, H.L. Cai, Y.B. Xu, D. Wu, G.D. Wang, A novel design: partitioning achieved by quenching and tempering (Q-T & P) in an aluminium-added low-density steel, *Scripta Mater.* 68 (2013) 370–374.
- [31] Y. Li, X. Li, G. Yuan, J. Kang, D. Chen, G. Wang, Microstructure and partitioning behavior characteristics in low carbon steels treated by hot-rolling direct quenching and dynamical partitioning processes, *Mater. Char.* 121 (2016) 157–165.
- [32] H. Liu, X. Lu, X. Jin, H. Dong, J. Shi, Enhanced mechanical properties of a hot stamped advanced high-strength steel treated by quenching and partitioning process, *Scripta Mater.* 64 (2011) 749–752.
- [33] F. Huang, J. Yang, Z. Guo, S. Chen, Y. Rong, N. Chen, Effect of partitioning treatment on the mechanical property of Fe-0.19C-1.47Mn-1.50Si steel with refined martensitic microstructure, *Metall. Mater. Trans. A* 47A (2016) 1072–1082.
- [34] C. Wang, Y. Chang, X. Li, K. Zhao, H. Dong, Relation of martensite-retained austenite and its effect on microstructure and mechanical properties of the quenched and partitioned steels, *Sci. China Technol. Sci.* 59 (2016) 832–838.
- [35] M.J. Santofimia, T. Nguyen-Minh, L. Zhao, R. Petrov, I. Sabirov, J. Sietsma, New low carbon Q&P steels containing film-like intercritical ferrite, *Mater. Sci. Eng., A* 527 (2010) 6429–6439.
- [36] W. Li, H. Gao, H. Nakashima, S. Hata, W. Tian, Microstructural evolution and mechanical properties of a low-carbon quenching and partitioning steel after partial and full austenitization, *Int. J. Min. Met. Mater.* 23 (2016) 906–919.
- [37] Y. Xu, X. Tan, X. Yang, Z. Hu, F. Peng, D. Wu, G. Wang, Microstructure evolution and mechanical properties of a hot-rolled directly quenched and partitioned steel containing proeutectoid ferrite, *Mater. Sci. Eng., A* 607 (2014) 460–475.
- [38] J. Zhang, H. Ding, R.D.K. Misra, Enhanced strain hardening and microstructural characterization in a low carbon quenching and partitioning steel with partial austenitization, *Mater. Sci. Eng., A* 636 (2015) 53–59.
- [39] X. Tan, Y. Xu, D. Pong, X. Yang, Z. Hu, F. Peng, X. Ju, D. Wu, D. Raabe, Effect of intercritical deformation on microstructure and mechanical properties of a low-silicon aluminum-added hot-rolled directly quenched and partitioned steel, *Mater. Sci. Eng., A* 656 (2016) 200–215.
- [40] G. Mandal, S.K. Ghosh, S. Bera, S. Mukherjee, Effect of partial and full austenitisation on microstructure and mechanical properties of quenching and partitioning steel, *Mater. Sci. Eng., A* 676 (2016) 56–64.
- [41] D. Yan, C.C. Tasan, D. Raabe, High resolution in situ mapping of microstrain and microstructure evolution reveals damage resistance criteria in dual phase steels, *Acta Mater.* 96 (2015) 399–409.
- [42] C.C. Tasan, M. Diehl, D. Yan, C. Zambaldi, P. Shanthraj, F. Roters, D. Raabe, Integrated experimental-simulation analysis of stress and strain partitioning in multiphase alloys, *Acta Mater.* 81 (2014) 386–400.
- [43] C.C. Tasan, J.P.M. Hoefnagels, M. Diehl, D. Yan, F. Roters, D. Raabe, Strain localization and damage in dual phase steels investigated by coupled in-situ deformation experiments and crystal plasticity simulations, *Int. J. Plast.* 63 (2014) 198–210.
- [44] M.M. Wang, J.C. Hell, C.C. Tasan, Martensite size effects on damage in quenching and partitioning steels, *Scripta Mater.* 138 (2017) 1–5.
- [45] B. Fu, W.Y. Yang, Y.D. Wang, L.F. Li, Z.Q. Sun, Y. Ren, Micromechanical behavior of TRIP-assisted multiphase steels studied with in situ high-energy X-ray diffraction, *Acta Mater.* 76 (2014) 342–354.
- [46] M. Koyama, Z. Zhang, M. Wang, D. Pong, D. Raabe, K. Tsuzaki, H. Noguchi, C.C. Tasan, Bone-like crack resistance in hierarchical metastable nanolaminate steels, *Science* 355 (2017) 1055–1057.
- [47] M.M. Wang, C.C. Tasan, D. Pong, D. Raabe, Spectral TRIP enables ductile 1.1 GPa martensite, *Acta Mater.* 111 (2016) 262–272.
- [48] M. Wang, C.C. Tasan, D. Pong, A. Kostka, D. Raabe, Smaller is less stable: size effects on twinning vs. transformation of reverted austenite in TRIP-maraging steels, *Acta Mater.* 79 (2014) 268–281.
- [49] L. Morsdorf, O. Jeannin, D. Barbier, M. Mitsuhashi, D. Raabe, C.C. Tasan, Multiple mechanisms of lath martensite plasticity, *Acta Mater.* 121 (2016) 202–214.
- [50] Z.J. Xie, S.F. Yuan, W.H. Zhou, J.R. Yang, H. Guo, C.J. Shang, Stabilization of retained austenite by the two-step intercritical heat treatment and its effect on the toughness of a low alloyed steel, *Mater. Des.* 59 (2014) 193–198.
- [51] B. Avishan, G. Garcia-Mateo, S. Yazdani, F.G. Caballero, Retained austenite thermal stability in a nanostructured bainitic steel, *Mater. Char.* 81 (2013) 105–110.
- [52] A.S. Podder, H.K.D.H. Bhadeshia, Thermal stability of austenite retained in bainitic steels, *Mater. Sci. Eng., A* 527 (2010) 2121–2128.
- [53] S. Djaziri, Y. Li, G.A. Nematollahi, B. Grabowski, S. Goto, C. Kirchlechner, A. Kostka, S. Doyle, J. Neugebauer, D. Raabe, G. Dehm, Deformation-induced martensite: a new paradigm for exceptional steels, *Adv. Mater.* 28 (2016) 7753–7757.
- [54] Y. Toji, H. Matsuda, D. Raabe, Effect of Si on the acceleration of bainite transformation by preexisting martensite, *Acta Mater.* 116 (2016) 250–262.

- [55] Y. Toji, H. Matsuda, M. Herbig, P. Choi, D. Raabe, Atomic-scale analysis of carbon partitioning between martensite and austenite by atom probe tomography and correlative transmission electron microscopy, *Acta Mater.* 65 (2014) 215–228.
- [56] K. Hono, D. Raabe, S.P. Ringer, D.N. Seidman, Atom probe tomography of metallic nanostructures, *MRS Bull.* 41 (2016) 23–29.
- [57] B.L. Ennis, E. Jimenez-Melero, R. Mostert, B. Santillana, P.D. Lee, The role of aluminium in chemical and phase segregation in a TRIP-assisted dual phase steel, *Acta Mater.* 115 (2016) 132–142.
- [58] H. Dong, X. Sun, Deformation induced ferrite transformation in low carbon steels, *Curr. Opin. Solid State Mater. Sci.* 9 (2005) 269–276.
- [59] L. Morsdorf, C.C. Tasan, D. Ponge, D. Raabe, 3D structural and atomic-scale analysis of lath martensite: effect of the transformation sequence, *Acta Mater.* 95 (2015) 366–377.
- [60] W. Song, J. von Appen, P. Choi, R. Dronskowski, D. Raabe, W. Bleck, Atomic-scale investigation of ϵ and θ precipitates in bainite in 100Cr6 bearing steel by atom probe tomography and ab initio calculations, *Acta Mater.* 61 (2013) 7582–7590.
- [61] M. Calcagnotto, D. Ponge, E. Demir, D. Raabe, Orientation gradients and geometrically necessary dislocations in ultrafine grained dual-phase steels studied by 2D and 3D EBSD, *Mater. Sci. Eng., A* 527 (2010) 2738–2746.
- [62] J. Kadkhodapour, S. Schmauder, D. Raabe, S. Ziaei-Rad, U. Weber, M. Calcagnotto, Experimental and numerical study on geometrically necessary dislocations and non-homogeneous mechanical properties of the ferrite phase in dual phase steels, *Acta Mater.* 59 (2011) 4387–4394.
- [63] C.C. Tasan, M. Diehl, D. Yan, M. Bechtold, F. Roters, L. Schemmann, C. Zheng, N. Peranio, D. Ponge, M. Koyama, K. Tsuzaki, D. Raabe, An overview of dual-phase steels: advances in microstructure-oriented processing and micro-mechanically guided design, in: D.R. Clarke (Ed.), *Annual Review of Materials Research*, vol. 45, 2015, pp. 391–431.
- [64] S. Fréhard, F. Martin, C. Clément, J. Cousty, AFM and EBSD combined studies of plastic deformation in a duplex stainless steel, *Mater. Sci. Eng., A* 418 (2006) 312–319.
- [65] W. Wang, T.G. Liu, X.Y. Cao, Y.H. Lu, T. Shoji, In-situ SEM study of crack initiation and propagation behavior in a dissimilar metal welded joint, *Mater. Sci. Eng., A* 729 (2018) 331–339.
- [66] K. Yvell, T.M. Grehk, P. Hedström, A. Borgenstam, G. Engberg, Microstructure development in a high-nickel austenitic stainless steel using EBSD during in situ tensile deformation, *Mater. Char.* 135 (2018) 228–237.
- [67] W.D. Callister Jr., *Fundamentals of Materials Science and Engineering*, John Wiley & Sons, Inc., New York, 2001.
- [68] J. Han, S. Lee, J. Jung, Y. Lee, The effects of the initial martensite microstructure on the microstructure and tensile properties of intercritically annealed Fe–9Mn–0.05C steel, *Acta Mater.* 78 (2014) 369–377.
- [69] K. Zhang, P. Liu, W. Li, Z. Guo, Y. Rong, Ultrahigh strength-ductility steel treated by a novel quenching-partitioning-tempering process, *Mater. Sci. Eng., A* 619 (2014) 205–211.
- [70] Z.J. Xie, Y.Q. Ren, W.H. Zhou, J.R. Yang, C.J. Shang, R.D.K. Misra, Stability of retained austenite in multi-phase microstructure during austempering and its effect on the ductility of a low carbon steel, *Mater. Sci. Eng., A* 603 (2014) 69–75.
- [71] Y.F. Shen, L.N. Qiu, X. Sun, L. Zuo, P.K. Liaw, D. Raabe, Effects of retained austenite volume fraction, morphology, and carbon content on strength and ductility of nanostructured TRIP-assisted steels, *Mater. Sci. Eng., A* 636 (2015) 551–564.
- [72] X.D. Wang, B.X. Huang, Y.H. Rong, L. Wang, Microstructures and stability of retained austenite in TRIP steels, *Mater. Sci. Eng., A* 438 (2006) 300–305.
- [73] J. Chiang, J.D. Boyd, A.K. Pilkey, Effect of microstructure on retained austenite stability and tensile behaviour in an aluminum-alloyed TRIP steel, *Mater. Sci. Eng., A* 638 (2015) 132–142.
- [74] S.G. Liu, S.S. Dong, F. Yang, L. Li, B. Hu, F.H. Xiao, Q. Chen, H.S. Liu, Application of quenching-partitioning-tempering process and modification to a newly designed ultrahigh carbon steel, *Mater. Des.* 56 (2014) 37–43.
- [75] E. Jimenez-Melero, N.H. van Dijk, L. Zhao, J. Sietsma, S.E. Offerman, J.P. Wright, S. van der Zwaag, Characterization of individual retained austenite grains and their stability in low-alloyed TRIP steels, *Acta Mater.* 55 (2007) 6713–6723.
- [76] H.S. Park, J.C. Han, N.S. Lim, J. Seol, C.G. Park, Nano-scale observation on the transformation behavior and mechanical stability of individual retained austenite in CMnSiAl TRIP steels, *Mater. Sci. Eng., A* 627 (2015) 262–269.
- [77] X.C. Xiong, B. Chen, M.X. Huang, J.F. Wang, L. Wang, The effect of morphology on the stability of retained austenite in a quenched and partitioned steel, *Scripta Mater.* 68 (2013) 321–324.
- [78] S.O. Kruijver, L. Zhao, J. Sietsma, S.E. Offerman, N.H. Van Dijk, E.M. Lauridsen, L. Margulies, S. Grigull, H.F. Poulsen, S. Van der Zwaag, In situ observations on the mechanical stability of austenite in TRIP-steel, *J. Phys. IV* 104 (2003) 499–502.